Biomedical Optics EXPRESS

Limitations to adaptive optics image quality in rodent eyes

Xiaolin Zhou*, Phillip Bedggood, and Andrew Metha

Department of Optometry and Vision Sciences, University of Melbourne, Australia
**zhoux@student.unimelb.edu.au*

Abstract: Adaptive optics (AO) retinal image quality of rodent eyes is inferior to that of human eyes, despite the promise of greater numerical aperture. This paradox challenges several assumptions commonly made in AO imaging, assumptions which may be invalidated by the very high power and dioptric thickness of the rodent retina. We used optical modeling to compare the performance of rat and human eyes under conditions that tested the validity of these assumptions. Results showed that AO image quality in the human eye is robust to positioning errors of the AO corrector and to differences in imaging depth and wavelength compared to the wavefront beacon. In contrast, image quality in the rat eye declines sharply with each of these manipulations, especially when imaging off-axis. However, some latitude does exist to offset these manipulations against each other to produce good image quality.

OCIS codes: (010.1080) Active or adaptive optics; (170.3880) Medical and biological imaging; (170.4460) Ophthalmic optics and devices.

References

1. B. V. Bui, B. Edmunds, G. A. Cioffi, and B. Fortune, "The gradient of retinal functional changes during acute intraocular pressure elevation," Invest. Ophthalmol. Vis. Sci. **46**(1), 202–213 (2005).
2. B. V. Bui, M. Loeliger, M. Thomas, A. J. Vingrys, S. M. Rees, C. T. Nguyen, Z. He, and M. Tolcos, "Investigating structural and biochemical correlates of ganglion cell dysfunction in streptozotocin-induced diabetic rats," Exp. Eye Res. **88**(6), 1076–1083 (2009).
3. K. Kohzaki, A. J. Vingrys, and B. V. Bui, "Early inner retinal dysfunction in streptozotocin-induced diabetic rats," Invest. Ophthalmol. Vis. Sci. **49**(8), 3595–3604 (2008).
4. Z. He, B. V. Bui, and A. J. Vingrys, "Effect of repeated IOP challenge on rat retinal function," Invest. Ophthalmol. Vis. Sci. **49**(7), 3026–3034 (2008).
5. R. E. Marc, B. W. Jones, C. B. Watt, F. Vazquez-Chona, D. K. Vaughan, and D. T. Organisciak, "Extreme retinal remodeling triggered by light damage: implications for age related macular degeneration," Mol. Vis. **14**, 782–806 (2008).
6. S. L. Mansour, K. R. Thomas, and M. R. Capecchi, "Disruption of the proto-oncogene int-2 in mouse embryo-derived stem cells: a general strategy for targeting mutations to non-selectable genes," Nature **336**(6197), 348–352 (1988).
7. M. R. Capecchi, "Altering the genome by homologous recombination," Science **244**(4910), 1288–1292 (1989).
8. A. Abbott, "Laboratory animals: the Renaissance rat," Nature **428**(6982), 464–466 (2004).
9. A. M. Geurts, G. J. Cost, Y. Freyvert, B. Zeitler, J. C. Miller, V. M. Choi, S. S. Jenkins, A. Wood, X. Cui, X. Meng, A. Vincent, S. Lam, M. Michalkiewicz, R. Schilling, J. Foeckler, S. Kalloway, H. Weiler, S. Ménoret, I. Anegon, G. D. Davis, L. Zhang, E. J. Rebar, P. D. Gregory, F. D. Urnov, H. J. Jacob, and R. Buelow, "Knockout rats via embryo microinjection of zinc-finger nucleases," Science **325**(5939), 433 (2009).
10. A. Roorda, "Applications of adaptive optics scanning laser ophthalmoscopy," Optom. Vis. Sci. **87**(4), 260–268 (2010).
11. P. Godara, A. M. Dubis, A. Roorda, J. L. Duncan, and J. Carroll, "Adaptive optics retinal imaging: emerging clinical applications," Optom. Vis. Sci. **87**(12), 930–941 (2010).
12. J. Liang, D. R. Williams, and D. T. Miller, "Supernormal vision and high-resolution retinal imaging through adaptive optics," J. Opt. Soc. Am. A **14**(11), 2884–2892 (1997).
13. Y. Geng, K. P. Greenberg, R. Wolfe, D. C. Gray, J. J. Hunter, A. Dubra, J. G. Flannery, D. R. Williams, and J. Porter, "In vivo imaging of microscopic structures in the rat retina," Invest. Ophthalmol. Vis. Sci. **50**(12), 5872–5879 (2009).

#165728 - $15.00 USD Received 3 Apr 2012; revised 8 Jun 2012; accepted 14 Jun 2012; published 3 Jul 2012

14. D. P. Biss, D. Sumorok, S. A. Burns, R. H. Webb, Y. Zhou, T. G. Bifano, D. Côté, I. Veilleux, P. Zamiri, and C. P. Lin, "In vivo fluorescent imaging of the mouse retina using adaptive optics," Opt. Lett. **32**(6), 659–661 (2007).
15. Y. Geng, A. Dubra, L. Yin, W. H. Merigan, R. Sharma, R. T. Libby, and D. R. Williams, "Adaptive optics retinal imaging in the living mouse eye," Biomed. Opt. Express **3**(4), 715–734 (2012).
16. A. Dubra, Y. Sulai, J. L. Norris, R. F. Cooper, A. M. Dubis, D. R. Williams, and J. Carroll, "Noninvasive imaging of the human rod photoreceptor mosaic using a confocal adaptive optics scanning ophthalmoscope," Biomed. Opt. Express **2**(7), 1864–1876 (2011).
17. Y. Geng, L. A. Schery, R. Sharma, A. Dubra, K. Ahmad, R. T. Libby, and D. R. Williams, "Optical properties of the mouse eye," Biomed. Opt. Express **2**(4), 717–738 (2011).
18. G. Smith and D. A. Atchison, *The Eye and Visual Optical Instruments* (Cambridge University Press, Cambridge, UK; New York, USA, 1997).
19. A. Hughes, "A schematic eye for the rat," Vision Res. **19**(5), 569–588 (1979).
20. A. Chan, J. S. Duker, T. H. Ko, J. G. Fujimoto, and J. S. Schuman, "Normal macular thickness measurements in healthy eyes using Stratus optical coherence tomography," Arch. Ophthalmol. **124**(2), 193–198 (2006).
21. A. Chaudhuri, P. E. Hallett, and J. A. Parker, "Aspheric curvatures, refractive indices and chromatic aberration for the rat eye," Vision Res. **23**(12), 1351–1363 (1983).
22. R. E. Bedford and G. Wyszecki, "Axial chromatic aberration of the human eye," J. Opt. Soc. Am. **47**(6), 564–565 (1957).
23. P. Bedggood and A. Metha, "System design considerations to improve isoplanatism for adaptive optics retinal imaging," J. Opt. Soc. Am. A **27**(11), A37–A47 (2010).
24. M. C. W. Campbell and A. Hughes, "An analytic, gradient index schematic lens and eye for the rat which predicts aberrations for finite pupils," Vision Res. **21**(7), 1129–1148, 1135–1148 (1981).
25. H. L. Liou and N. A. Brennan, "Anatomically accurate, finite model eye for optical modeling," J. Opt. Soc. Am. A **14**(8), 1684–1695 (1997).
26. G. Smith, P. Bedggood, R. Ashman, M. Daaboul, and A. Metha, "Exploring ocular aberrations with a schematic human eye model," Optom. Vis. Sci. **85**(5), 330–340 (2008).
27. A. V. Goncharov and C. Dainty, "Wide-field schematic eye models with gradient-index lens," J. Opt. Soc. Am. A **24**(8), 2157–2174 (2007).
28. M. Born and E. Wolf, *Principles of Optics: Electromagnetic Theory of Propagation, Interference and Diffraction of Light* (Cambridge University Press, Cambridge; New York, 1999).
29. S. Remtulla and P. E. Hallett, "A schematic eye for the mouse, and comparisons with the rat," Vision Res. **25**(1), 21–31 (1985).
30. E. J. Fernández, A. Unterhuber, P. M. Prieto, B. Hermann, W. Drexler, and P. Artal, "Ocular aberrations as a function of wavelength in the near infrared measured with a femtosecond laser," Opt. Express **13**(2), 400–409 (2005).
31. S. Marcos, S. A. Burns, E. Moreno-Barriusop, and R. Navarro, "A new approach to the study of ocular chromatic aberrations," Vision Res. **39**(26), 4309–4323 (1999).
32. P. Artal, E. Berrio, A. Guirao, and P. Piers, "Contribution of the cornea and internal surfaces to the change of ocular aberrations with age," J. Opt. Soc. Am. A **19**(1), 137–143 (2002).
33. A. B. Metha, A. M. Crane, H. G. Rylander 3rd, S. L. Thomsen, and D. G. Albrecht, "Maintaining the cornea and the general physiological environment in visual neurophysiology experiments," J. Neurosci. Methods **109**(2), 153–166 (2001).
34. A. Roorda, F. Romero-Borja, W. Donnelly Iii, H. Queener, T. Hebert, and M. Campbell, "Adaptive optics scanning laser ophthalmoscopy," Opt. Express **10**(9), 405–412 (2002).
35. P. A. Bedggood, *Adaptive Optics Methods to Increase the Isoplanatic Patch Size for Human Retinal Imaging*, (Dept. of Optometry and Vision Sciences, University of Melbourne, 2008)
36. H. Hofer, N. Sredar, H. Queener, C. Li, and J. Porter, "Wavefront sensorless adaptive optics ophthalmoscopy in the human eye," Opt. Express **19**(15), 14160–14171 (2011).
37. D. Débarre, E. J. Botcherby, T. Watanabe, S. Srinivas, M. J. Booth, and T. Wilson, "Image-based adaptive optics for two-photon microscopy," Opt. Lett. **34**(16), 2495–2497 (2009).
38. D. P. Biss, R. H. Webb, Y. Zhou, T. G. Bifano, P. Zamiri, and C. P. Lin, "An adaptive optics biomicroscope for mouse retinal imaging," Proc. SPIE **6467**, 646703, 646703-8 (2007).
39. S. Zommer, E. N. Ribak, S. G. Lipson, and J. Adler, "Simulated annealing in ocular adaptive optics," Opt. Lett. **31**(7), 939–941 (2006).

1. Introduction

Rodents are commonly used in eye disease models such as glaucoma, diabetes and macular degeneration due to their low cost, ease of maintenance and handling, and rapid growth compared to primates [1–5]. Targeted gene manipulation techniques are also well established in mice [6,7] and have recently become tractable in rats [8,9], making rodent models an indispensible tool for the study of eye disease. Adaptive optics (AO) allows diffraction-limited imaging of the retina, which provides non-invasive visualization of disease models on the microscopic scale, and their evolution over time, in living eyes [10,11]. Adaptive optics

#165728 - $15.00 USD Received 3 Apr 2012; revised 8 Jun 2012; accepted 14 Jun 2012; published 3 Jul 2012

has been used successfully in human eyes for the past 15 years [12], and offers even greater potential in rodent eyes which have more than twice the numerical aperture when pupils are maximally dilated [13].

Several studies have attempted to image the rodent eye with AO, allowing visualization of the photoreceptor mosaic in reflectance and of ganglion cell features in fluorescence [13–15]. Despite the theoretically superior resolution in the rodent eye, published images have until recently suffered from significantly reduced contrast and resolution compared to the state of the art in primate and human eyes [10,11,16].

The reduced quality of AO images in the rodent eye has previously been attributed to non-optimized defocus and failure of the wavefront sensor to capture all sources of image blur due to separation between wavefront sensing and imaging planes [13]. To overcome this problem Geng et al. (2011) presented a modified system to improve the fidelity of wavefront measurements in the mouse eye [17]. This system adopted several modifications to improve the axial resolution of the wavefront sensor, minimizing Shack-Hartmann spot distortion that arises from the combination of high eye power with the multiple sites of reflectance of the wavefront beacon.

Recently these efforts have been rewarded with superior quality in published images compared to previous data [15]. However, to our knowledge consistently obtaining such images is not yet routine, and contrast and resolution are still lower than what is theoretically achievable, especially in reflectance imaging. Obtaining high quality images in the rodent eye remains a challenging enterprise.

An oft-made approximation in AO imaging is to adjust for differences in the imaging plane or the imaging wavelength, compared to the wavefront beacon, by altering low-order spherical defocus alone. This can be achieved by moving the camera, or using the AO corrector itself, a movable Badal system, or trial lenses. In doing so, it is presumed that higher order aberrations such as astigmatism, coma and spherical aberration (SA) change by a negligible amount. However, these aberrations scale rapidly with eye power (to the first, second and third powers, respectively [18]. In addition the dioptric thickness of the rodent retina is large compared to human eyes (~11 D in the rat compared to ~0.7 D in human [19,20]); likewise the chromatic aberration in the rodent eye is much larger than in the human (~6 D in the rat compared to ~1 D in the human over 475-650 nm [21,22]). These factors may render this approximation invalid for rodent eyes. Similarly, in human eyes there is little consequence when the AO corrector is not precisely conjugate to the exit pupil [23]; this may not be the case for much more highly powered rodent eyes.

In this work we compare residual aberrations between rat and human schematic eyes under the above manipulations, in order to understand and improve upon the relatively poor images often obtained during AO imaging of rodent eyes.

2. Methods

The optical design software ZEMAX (Zemax Development Corporation) was used to model AO correction of both rat and human schematic eyes.

2.1. Rat schematic eye parameters

The rat schematic eye used in this study was developed using parameters from two previous studies. Radius of curvature and gradient index lens (GRIN) data were obtained from Campbell and Hughes (1981) [24], with a 3.5 mm diameter exit pupil. Dispersion and surface asphericity data were obtained from Chaudhuri et al. (1983) [21]. The parameters used are summarized in Tables 1 & 2.

#165728 - $15.00 USD Received 3 Apr 2012; revised 8 Jun 2012; accepted 14 Jun 2012; published 3 Jul 2012

Table 1. Parameters of the rat schematic eye used in the modeling, modified from Campbell and Hughes (1981)

Surface	n (550 nm)	Radius of curvature (mm)	Distance between surfaces (mm)	Conic constant
Ant cornea		–2.965		0.796
	1.3838		0.26	
Post cornea		–2.705		0.407
	1.3346		0.62	
Ant lens		–2.34		0.181
GRIN	1.5034 (lens core)		3.71	
Post lens		2.34		0.268
	1.3358		1.39	
ILM		3.624*		n/a
	1.3358		0.17	
OLM		3.624*		n/a

ILM: inner limiting membrane; OLM: outer limiting membrane.
*Chaudhuri, Hallett et al. 1983 [21].

Table 2. Dispersion data for the rat schematic eye, modified from Chaudhuri et al. (1983)

	Wavelength (nm)							
	475	**500**	**525**	**550**	**575**	**600**	**625**	**650**
Cornea	1.3882	1.3864	1.3848	1.3838	1.3829	1.3821	1.3812	1.3804
Aqueous	1.3381	1.3366	1.3355	1.3346	1.3336	1.3329	1.3321	1.3315
Vitreous	1.3379	1.3367	1.3358	1.3349	1.3341	1.3332	1.3322	1.3319
Lens Cortex (r = 1)	1.4715	1.4700	1.4684	1.4669	1.4657	1.4644	1.4635	1.4627
Lens Core (r = 0)	1.5105	1.5079	1.5055	1.5034	1.5016	1.4998	1.4985	1.4974

Note that for Table 1, all values were obtained from Campbell and Hughes (1981) [24] unless stated otherwise. For Table 2, refractive indices were averaged from measurements of freshly excised samples with both the Zeiss Abbé refractometer and the Jena Interphako image-splitting interference microscope [21]. The original values for the bottom two rows were shifted by a fixed amount to match that from Campbell and Hughes (1981) at 589 nm.

Refractive index variation of the Campbell and Hughes GRIN lens is described by Eq. (1):

$$n(r) = A - \frac{r^2}{B}, \tag{1}$$

where $n(r)$ represents the refractive index at a distance r mm from the centre of the lens [24]. The constants A and B depend on the wavelength being considered; A is the refractive index at the lens core and is given by the bottom row of Table 2. The second-bottom row of Table 2 was substituted into Eq. (1) to give the value of B at each wavelength.

2.2. Human schematic eye

The Liou and Brennan (1997) schematic human eye was used, with a 6 mm diameter exit pupil. This eye is anatomically representative, with aspheric surfaces and a gradient index lens [25]. The parameters are shown in Table 3 (with the exception of the radius of curvature of the retina, which is adopted from Smith et al. [26]). A viable alternative is the Goncharov and Dainty wide-field schematic eye, which also features a gradient index lens and has similar advantages to the Liou and Brennan eye [27].

#165728 - $15.00 USD Received 3 Apr 2012; revised 8 Jun 2012; accepted 14 Jun 2012; published 3 Jul 2012

Table 3. Parameters of the Liou and Brennan (1997) schematic human eye

Surface	n (555 nm)	Radius of curvature (mm)	Distance between surfaces (mm)	Conic constant	n_{00}	n_{01}	n_{02}	n_{10}
Ant cornea		–7.77		–0.18				
	1.376		0.5					
Post cornea		–6.4		–0.60				
	1.336		3.16					
Ant lens		–12.4		–0.94				
Ant GRIN	1.368		1.59		1.368	0.04906	–0.01543	–0.001978
GRIN Junction								
Post GRIN	1.368		2.43		1.407	0	–0.006605	–0.001978
Post lens		8.1		0.96				
	1.336		16.27					
ILM		12.0*		n/a				
	1.336		0.25					
OLM		12.0*		n/a				

ILM: inner limiting membrane; OLM: outer limiting membrane.
*Smith et al. (2008) [26]

The GRIN of this schematic eye is separated into anterior and posterior segments; each is described by Eq. (2):

$$n(w,z) = n_{00} + n_{01}z + n_{02}z^2 + n_{10}w^2, \quad (2)$$

where z is along the optical axis, w is the radial distance perpendicular to the z axis, and the n_{00}, n_{01}, n_{02}, n_{10} coefficients are given in Table 2 [25].

In addition, the dispersion properties of the ocular media are described by Eq. (3) [25]:

$$n(\text{media at } \lambda \text{ nm}) = n(\text{media at } 555\text{nm}) + 0.0512 - 1.455\times10^{-4}\lambda + 9.61\times10^{-8}\lambda^2, \quad (3)$$

where n(media at λ nm) is the resultant refractive index of the ocular media at λ nm, and n(media at 555 nm) is a reference refractive index at 555 nm.

2.3. Optical modeling

A phase plate in the exit pupil was used to model the AO corrector. Rays were traced out of the eye from a point on the retina. Rays were first traced through the entire ocular media before being refracted by the phase plate. This set-up removed the need for an optical relay system, so that best-case performance of the eyes could be evaluated. A paraxial lens was used to simulate image formation on a retinal camera. The wavefront beacon was nominally 650 nm and situated axially in the plane of the inner limiting membrane (ILM). The phase profile of this corrector is specified with Zernike wavefront coefficients, which were optimized by trial and error using the in-built Zemax optimization functions to achieve minimum residual wavefront error.

The residual root mean square (RMS) wavefront error based on a 6th order Zernike fit was used as a measure of image quality. Exit pupil size was 3.5 mm in the rat eye and 6.0 mm in the human eye. The image was considered diffraction-limited when the total RMS was < λ/14 (the Maréchal criterion) [28]. All calculations were made on-axis and at a variety of off-axis points; eccentricities are specified in system space: i.e., 1° off-axis in system space is equivalent to 0.5° and 0.8° in retinal space for the rat and human schematic eyes, respectively.

After best AO correction was achieved for 650 nm at the ILM, residual aberrations were calculated under three common manipulations, as described below and depicted in Fig. 1. For

#165728 - $15.00 USD Received 3 Apr 2012; revised 8 Jun 2012; accepted 14 Jun 2012; published 3 Jul 2012

each manipulation, defocus was re-optimized by moving the position of the camera, to simulate typical procedure in AO imaging of an eye. In all cases this was found to be precisely equivalent to adjusting only the defocus component of the AO corrector when it was in the exit pupil plane.

It is worth emphasizing that in a real system, the wavefront sensor would be effectively blind to the manipulations modeled here. This means that the AO correction would appear to be of high quality, with very low residual wavefront error, even though the quality of the image may be substantially degraded.

2.3.1. Varying the imaging plane through the entire retinal thickness

It is typical to assume that offsets in imaging plane depth relative to the wavefront beacon require only axial re-positioning of the science camera, or equivalently alteration of the defocus introduced by the corrector. Because the retina is so thin relative to the refracting ocular components in the human eye, other induced aberrations are typically considered negligible.

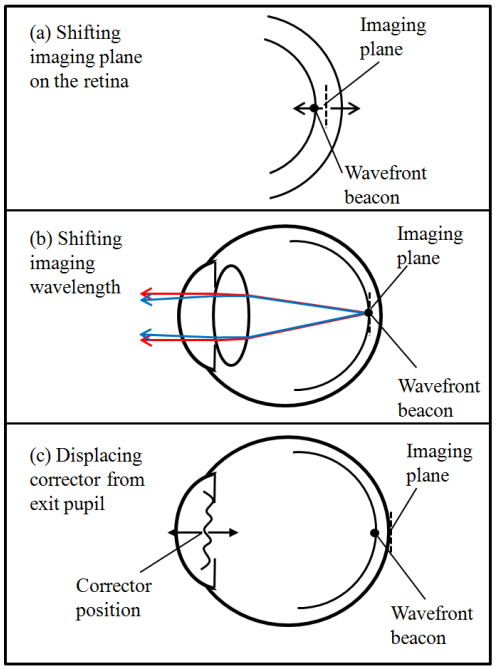

Fig. 1. A schematic depicting the manipulation of key AO imaging parameters. (a) The imaging plane was shifted from the ILM to the outer retina, assuming an average retinal thickness of 170 µm for the rat and 250 µm for the human eye. (b) The imaging wavelength was shifted from 650 nm (matching the wavefront sensing wavelength) to 475 nm. (c) The position of the AO corrector relative to the exit pupil was shifted. This manipulation exacerbates existing error, as opposed to introducing its own error; therefore baseline error was introduced by separating the imaging and sensing planes by the full retinal thickness as in (a).

We explored this assumption by first determining the AO correction for a wavefront beacon at the ILM. Keeping the AO corrector in this state, we then modeled variations in imaging plane position through the entire retinal thickness of 170 µm for the rat eye [19] and 250 µm for the human eye [20]. For each plane the science camera was re-positioned to minimize residual RMS wavefront error, which was recorded against retinal depth. For the human eye, only the point at the centre of the image was considered at each eccentricity. For the rat eye, both the central point and the average of 4 ‘edge’ points, 1° from the centre (i.e. a 2° diameter field of view), were considered, to explore anisoplanatic effects.

#165728 - $15.00 USD Received 3 Apr 2012; revised 8 Jun 2012; accepted 14 Jun 2012; published 3 Jul 2012

2.3.2. Varying imaging wavelength from 475 to 650 nm

The wavefront sensing and imaging lights are often of different wavelengths in AO imaging, allowing efficient channel separation using dichroic mirrors. The imaging wavelength can differ by up to 300-400 nm depending on the structure of interest; this difference is typically assumed to manifest as a shift in defocus that, as in case 1 above, can be corrected either by adjusting the science camera position or the second-order defocus term applied to the AO corrector.

We explored this assumption by first determining the AO correction for a 650 nm wavefront beacon (positioned at the ILM). Keeping the AO corrector in this state, we systematically modeled the effects of varying the imaging wavelength over a range from 650 to 475 nm. For each wavelength the science camera was re-positioned, to minimize residual RMS wavefront error. For the human eye, only the point at the centre of the image was considered at each eccentricity. For the rat eye, both the central point and the average of 4 'edge' points, 1° from the centre (i.e. a 2° diameter field of view), were considered, to explore anisoplanatic effects.

2.3.3. Displacing the AO corrector from the exit pupil plane

Although efforts are typically made to make both the AO corrector and the exit pupil of the eye conjugate to the pupil of the system, it is usually assumed that error of a few millimeters will not compromise image quality. This is certainly our experience in the human eye. From an initial condition of imaging at the same plane and wavelength as the wavefront beacon, we shifted the AO corrector axially from the exit pupil in small steps; little effect on wavefront quality was found. However, further modeling revealed a significant second-order effect whereby existing errors became exacerbated. We therefore separated the sensing and imaging planes by the full retinal thickness as in case 1 above, inducing a baseline level of residual aberration, to evaluate the additional effect of AO corrector mis-positioning. Throughout this manipulation, the corrector diameter was adjusted at each position so that vignetting did not affect wavefront correction. A low initial RMS wavefront error (<0.05 waves) was obtained at all corrector positions after wavefront correction. The residual RMS was recorded against corrector position for the central image point for both eye models.

3. Results

3.1. Shifting the imaging plane through the entire retinal thickness.

Figure 2 shows, for the human eye, the residual image plane wavefront RMS as a function of axial displacement relative to the wavefront beacon. Only data for the central image points are shown. Diffraction-limited performance was obtained through the entire retinal thickness out to almost 50° off-axis, where induced astigmatism began to limit image quality.

In contrast, Fig. 3 shows the results for the rat eye. In addition to the central image points considered for the human eye, here the average residual RMS at the edge of a 2° diameter field is also shown (open symbols). It can be seen that residual RMS at the edge of the field does not change significantly with separation between sensing and imaging planes; instead the effect is primarily a degradation of central image quality. Astigmatism rises linearly with axial error and quadratically with field position [18], and its contribution to residual RMS here rose from ~35% at 10° off-axis (the remainder was residual SA and higher order aberrations) to ~90% at 40° off-axis. Coma and SA did not contribute significantly to residual RMS at eccentricities >10°. Beyond about 15° off-axis (not plotted), a plane shift equivalent to the full retinal thickness was not able to be made diffraction-limited by changing defocus only.

#165728 - $15.00 USD Received 3 Apr 2012; revised 8 Jun 2012; accepted 14 Jun 2012; published 3 Jul 2012

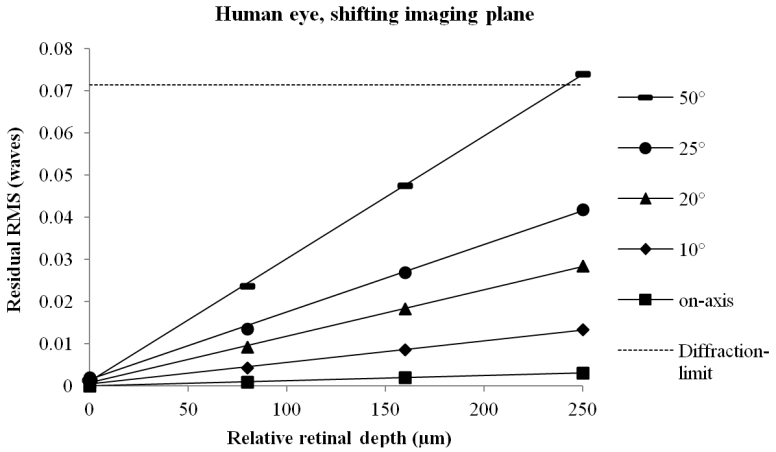

Fig. 2. Human eye: Effect of separation between imaging and sensing planes after optimizing for defocus. Residual wavefront RMS for selected image planes within the 250 µm human retina is plotted against separation from the sensing plane (which was located at the ILM). Exit pupil size: 6.0 mm. Diffraction limit was calculated according to the Maréchal criterion (λ/14; horizontal dashed line).

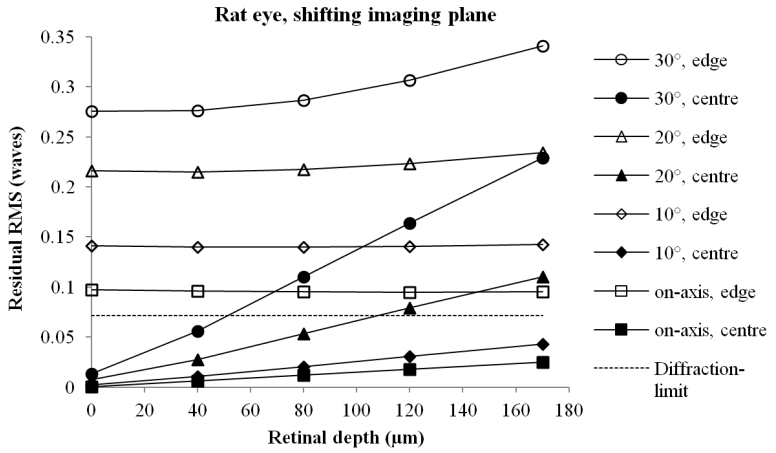

Fig. 3. Rat eye: Effect of separation between imaging and sensing planes after optimizing for defocus. Residual wavefront RMS for selected image planes within the 170 µm rat retina is plotted against separation from the sensing plane (which was located at the ILM). Closed symbols: centre of imaged field. Open symbols: edge of imaged field (averaged wavefront RMS from 4 points at edge of 2° diameter field). Exit pupil size: 3.5 mm. Diffraction limit was calculated according to the Maréchal criterion (λ/14; horizontal dashed line).

3.2. Shifting imaging wavelength from 475 to 650 nm.

Figure 4 shows, for the human eye, the image plane wavefront RMS at the central image point as a function of the wavelength difference between the sensing and imaging lights. Here the shifts in wavelength over the 175 nm range explored had relatively little impact on image quality at eccentricities less than 20°. Beyond this, astigmatism limited image quality, which accounted for ~65% of the residual RMS. The second largest contribution beyond 20° came from coma, which was ~35% at 30° and ~20% at 50°.

In contrast, Fig. 5 shows the results for the rat eye. In addition to the central field points (closed symbols), the average residual RMS at the edge of a 2° diameter field is shown (open symbols). It can be seen that changes in wavelength cause rapid degradation of both central and peripheral image quality. Residual coma was the limiting aberration at below 20° off-axis,

#165728 - $15.00 USD Received 3 Apr 2012; revised 8 Jun 2012; accepted 14 Jun 2012; published 3 Jul 2012

which ranged from ~60% at 10° off-axis to ~40% at 30° off-axis. There was also an increasing contribution from astigmatism due to its quadratic dependence on field position, which ranged from ~8% at 10° off-axis to ~45% at 30° off-axis. Spherical aberration was the limiting aberration on-axis. The tolerance on diffraction-limited imaging was Δλ ~25-75 nm for the eccentricities shown here.

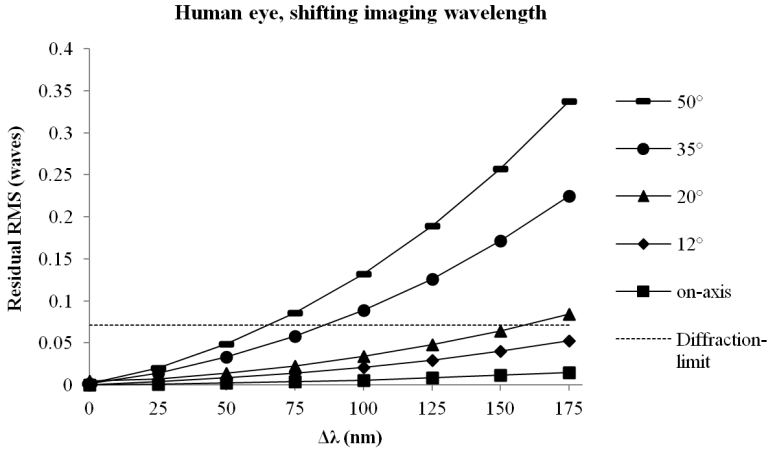

Fig. 4. Human eye: Effect of separation between imaging and sensing wavelengths after optimizing for defocus. Residual wavefront RMS is plotted as a function of the sensing-to-imaging wavelength difference, Δλ. Exit pupil size: 6.0 mm. Diffraction limit was calculated according to the Maréchal criterion (λ/14), which is represented as a horizontal dashed line.

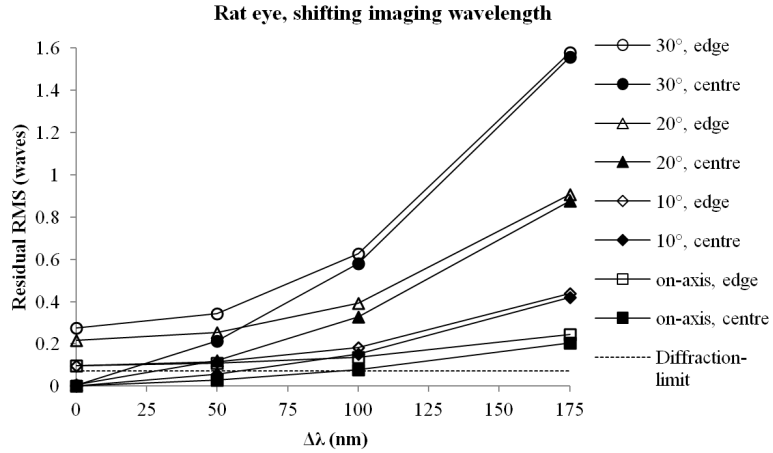

Fig. 5. Rat eye: Effect of difference between imaging and sensing wavelengths after optimizing for defocus. Residual wavefront RMS is plotted as a function of the sensing-to-imaging wavelength difference, Δλ. Closed symbols: centre of imaged field. Open symbols: edge of imaged field (averaged wavefront RMS from 4 points at edge of 2° diameter field). Exit pupil size: 3.5 mm. Diffraction limit was calculated according to the Maréchal criterion (λ/14; horizontal dashed line).

3.3. Displacing the AO corrector from the exit pupil plane.

Figure 6 shows, for the human eye, residual wavefront RMS for the central image point in the presence of axial separation of the AO corrector from the exit pupil plane. A baseline level of wavefront error was induced by separating the sensing and imaging planes by the full 250 μm retinal thickness, indicated by the data points at 0 mm corrector displacement. Axial displacement of the corrector away from the pupil then exacerbated this baseline error.

#165728 - $15.00 USD Received 3 Apr 2012; revised 8 Jun 2012; accepted 14 Jun 2012; published 3 Jul 2012

At smaller eccentricities, there was a large tolerance on corrector position to achieve diffraction-limited imaging. At larger eccentricities, some residual error was introduced (mainly astigmatism). The minimum that is evident for corrector positions slightly posterior to the pupil plane is unlikely to be of specific significance for real eyes; it depends on good centration of the refracting surfaces, and its sign becomes reversed upon reversal of the positions of the sensing and imaging planes.

Figure 7 shows the same results for the rat eye (full retinal thickness = 170 μm). The tolerance on corrector position is dramatically reduced in the rat eye; note the difference in scale on the horizontal axis. Axial shifting of corrector position had a roughly constant effect on the residual RMS regardless of eccentricity, as evidenced by the similarity of the shape of the curves, particularly at 20° and below. The similarity results from a consistent amount of residual SA, regardless of eccentricity. At a given corrector position, induced coma and

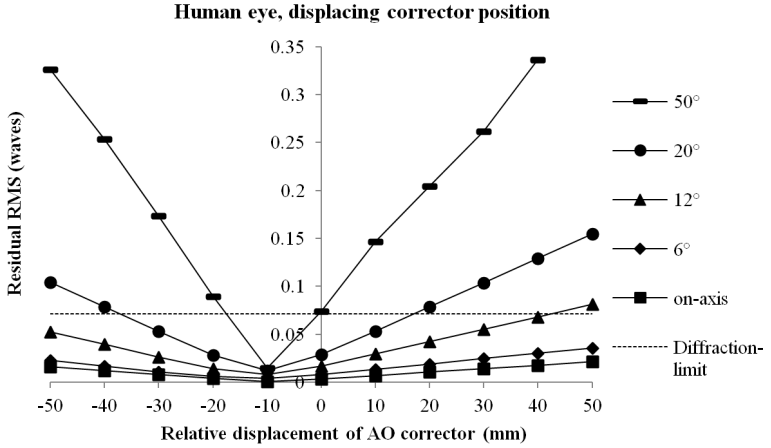

Fig. 6. Human eye: Effect of error in corrector position, in the presence of separation between imaging and sensing planes, and after optimizing for defocus. Residual wavefront RMS induced is plotted as a function of corrector separation from the exit pupil. Exit pupil size: 6.0 mm. Diffraction limit was calculated according to the Maréchal criterion (λ/14; horizontal dashed line).

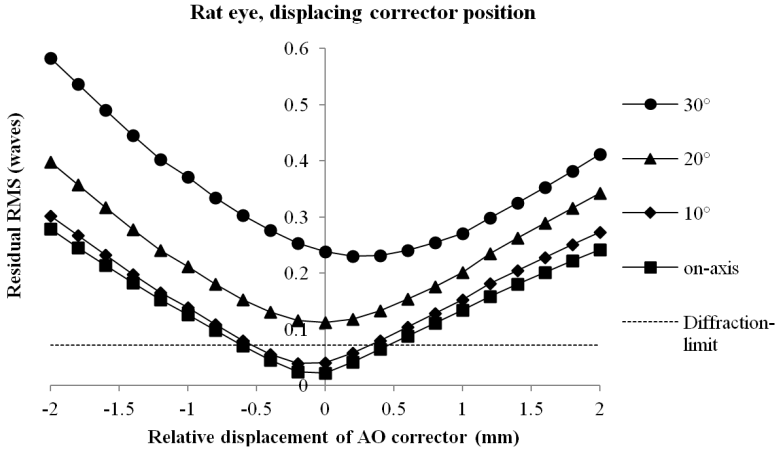

Fig. 7. Rat eye: Effect of error in corrector position in the presence of separation between imaging and sensing planes, and after optimizing for defocus. Only central image points are shown. Residual wavefront RMS induced is plotted as a function of corrector separation from the exit pupil. Exit pupil size: 3.5 mm. Diffraction limit was calculated according to the Maréchal criterion (λ/14; horizontal dashed line).

#165728 - $15.00 USD Received 3 Apr 2012; revised 8 Jun 2012; accepted 14 Jun 2012; published 3 Jul 2012

astigmatism approached SA in magnitude at ~30°. Tolerance on corrector position, approximated as axial shifts that changed RMS by no more than λ/14, was about ± 0.5 mm for the rat eye.

3.4. Combining the three sources of error to improve image quality.

Although the manipulations described above degraded image quality, it is possible to improve performance substantially by combining them in such a way that their aberration contributions are opposite in sign. We believe this offers some explanation for the high quality images that are able to be acquired in rodent eyes under certain conditions [15].

To demonstrate this point in the rat eye, we separated sensing and imaging planes by the full retinal thickness, and separated sensing and imaging wavelengths by the full spectral difference modeled above (i.e. sensing at the ILM at 650 nm, imaging at outer retina at 475 nm). We then systematically varied corrector position. Total residual RMS on-axis is plotted as the solid line in Fig. 8. It can be seen that despite poor image quality with the corrector at the pupil, displacing the corrector by <1 mm significantly improved performance.

The reason for this effect can be understood by considering the dashed lines in Fig. 8, which show the contributions to 4th order SA from the two individual sources of primary error (the addition of which precisely matched the total 4th order SA). There was a simple linear relationship between corrector position and induced SA for each source of error. Even though the slope of each component here is the same sign, the differences in their vertical position allow the existence of a zero solution for total 4th order SA. Due to the presence of higher order SA as well, the overall waverfront RMS (solid line) does not reach zero in this case. Off-axis points (not plotted) showed similarly shaped curves to Fig. 8, but were displaced both upwards and horizontally by an amount that depended on eccentricity (as is also evident in Fig. 7). In other words, the adjustment of corrector position offered significant benefit across all eccentricities considered, but the diffraction limit could often not be reached.

Interestingly, the direction of the slope of the component curves reverses upon reversal of the imaging/sensing planes or the imaging/sensing wavelengths (not shown). This will have a significant effect on the corrector position at which minimum RMS occurs; the best corrector position in practice is likely best decided by trial and error for a given imaging setup and a given eye.

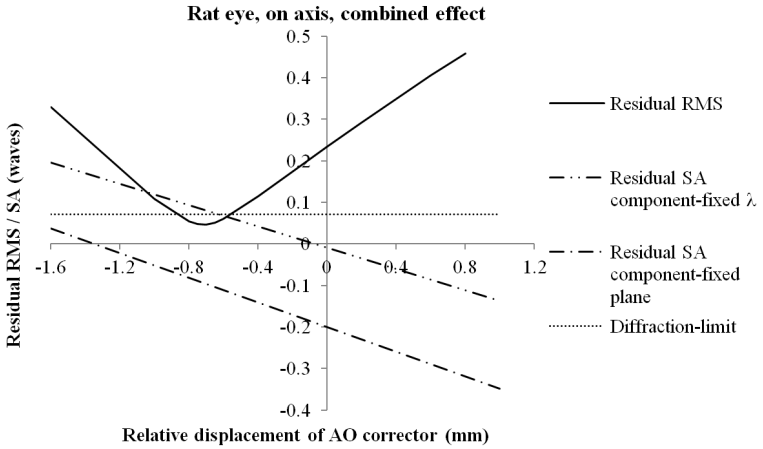

Fig. 8. Rat eye: Effect of error in corrector position, combining the three manipulations. Wavefront sensing and AO correction at 650 nm at the ILM. Imaging at 475 nm at the outer retina, after optimizing for defocus only. Solid curve: residual wavefont RMS; dot-dashed lines: residual SA components resulting from separation between imaging/sensing plane and wavelength. Exit pupil size: 3.5 mm. Diffraction limit was calculated according to the Maréchal criterion (λ/14; horizontal dashed line).

#165728 - $15.00 USD Received 3 Apr 2012; revised 8 Jun 2012; accepted 14 Jun 2012; published 3 Jul 2012

4. Discussion

In AO imaging of the human eye, it is customary to assume that differences in image plane and/or wavelength relative to the wavefront sensor can be compensated by simply altering defocus, without loss of image quality. It is also customary to assume that the AO corrector can be positioned 'loosely' in the pupil plane, with accuracy of a few millimeters. Our modeling confirms these assumptions to hold well for the human eye but to break down significantly for highly powered eyes such as the rat, especially at eccentric retinal locations. The effective optical axis in rodent eyes lies close to the optic nerve head [29]; imaging close to this area will therefore be least affected by the sources of error identified here. The effects are pronounced across the imaged field in the case of differences in wavelength, but primarily affect the central image area when sensing and imaging planes are separated. These considerations have a profound effect on the image quality that may be achieved in highly powered animal eyes in a given area of the retina.

It would be desirable to use analytical principles such as Seidel theory to generate rules of thumb to predict the magnitude of these errors for eye models from a range of animal species, or for different eyes in the same species. For example, such a rule may have allowed the prediction of some of our results from published experimental data that measured the change in higher order aberrations with wavelength in the human eye [30,31]. Conventional rules of thumb are not immediately applicable since we are dealing with the residual aberration left after a wavefront-guided adaptive correction, as distinct from some baseline level of aberration. New rules of thumb can often be generated by making approximations when the incident or emerging rays are collimated, when the refracting media are close together and close to the pupil plane, and when the gradient index contribution is small [18]. However none of these conditions hold true for rodent eyes, making the use of numerical ray tracing software necessary.

There is a moderate degree of uncertainty in the validity of rodent eye models, due to high variability in biometric parameters reported in the literature coupled with the rarity of published aberration data. In addition, parameters such as refraction and anterior corneal shape may vary markedly across the population. Due to the lack of a simple analytical expression, it is not immediately apparent how such variations might affect the generality of our conclusions. We therefore investigated this consideration empirically: we varied axial length over a 20 D range of refractive error, anterior corneal curvature over the range of measured normal population data [19], and compared a spherical anterior cornea to the aspheric cornea of our model. Despite these variations, which produced very large differences in *baseline* levels of aberration, comparatively little difference in *residual* aberrations were obtained for the sources of error considered here (e.g. at 20° off-axis, steepening the anterior corneal curvature by 2 standard deviations from the mean altered residual RMS by ~15% for the full separation between imaging and sensing planes, with curves highly similar in shape to the results shown above). This exercise improves our confidence that our conclusions will hold valid for most rat eyes.

Since changes in individual surface parameters seem to minimally affect our results, much of the difference between rat and human eyes is likely to result from their different equivalent powers (with significant contributions also likely to stem from differences in dioptric thickness of the retina and chromatic aberration). If this is true, efforts to neutralize the power of the cornea will provide significant reduction of residual aberrations. Note that this may actually cause an increase in baseline aberration level if the cornea and lens tend to contribute in opposing sign to total eye aberration, as has been shown to occur in the human eye [32]. The cornea is commonly flattened with a microscope coverslip for rodent retinal imaging studies, and this has been employed in AO imaging of the rodent eye previously [14]. However for imaging sessions longer than an hour the effects of hypoxia on the corneal

#165728 - $15.00 USD Received 3 Apr 2012; revised 8 Jun 2012; accepted 14 Jun 2012; published 3 Jul 2012

epithelium and stroma would likely be detrimental to optical quality [33]. A saline immersion method or gas permeable cover slip could prove even more useful.

Although these considerations are far less important for imaging human eyes, they are not completely immune to the errors mentioned above. Beyond 20° off-axis, the full separation between sensing and imaging wavelengths modeled here caused image quality to become limited by residual aberrations, despite defocus optimization. Combined with errors in corrector position and offset between imaging and sensing planes, residual aberrations could become a limiting factor for less eccentric retinal locations. This may partly explain the typically reduced image quality obtained when imaging the peripheral human retina with AO [16].

There are several potential ways to overcome the sources of error identified here. As shown in the combined series of manipulations of Fig. 8, when error is present both due to shifts in image plane and wavelength, it is possible to minimize residual RMS by varying corrector position. This is simple to do in practice, as the animal need only be translated axially while observing the effect on image quality. Indeed, most investigators in rodent AO imaging pay careful attention to the axial positioning of the animal, far more so than in the human eye. This finding may help to explain why this is the case.

Another potential solution is to systematically compensate for individual contributing aberrations. For example, in a centered eye the astigmatism is a linear function of field position [18]. When error is introduced between sensing and imaging planes, the magnitude of the astigmatism is altered while the axis remains constant. Therefore keeping the corrector's axis of astigmatism fixed and varying the magnitude, while observing image quality, could allow minimization of this source of error. We attempted this in practice in reflectance imaging on a real rat eye and found little benefit, probably because the rat eye is not well centered and because of concurrent chromatic errors.

Although recent images of ganglion cells were obtained using a $\Delta\lambda = 380$ nm [15], further benefit is expected from the use of a similar sensing wavelength to the desired imaging wavelength; ideally they would be the same. Confocal scanning systems have an inherent advantage here, since the wavefront sensing and imaging sources are often made to be the same [34]. The sensing plane should also be as similar as possible in depth to the desired imaging plane. Geng et al. (2011) employed a large, annular beam with vergence control to deliver their wavefront sensing light, permitting reflections from retinal layers outside the plane of interest to be disregarded [17]. This technique was primarily directed to improve the quality of the Shack-Hartmann spots, but the above logic predicts additional benefits.

One way to ensure that sensing and imaging occur at the same plane/wavelength is to use fluorescent labels to provide the light for both tasks. This was previously employed by Biss, et al (2007) [14] for another purpose (again to improve the appearance of the Hartmann-Shack spots). As long as the targets labeled are confined to a distinct retinal layer, this will solve both primary types of error reported above, and so also remove the secondary error incurred with AO corrector mis-positioning.

In the event that the primary sources of error (in sensing wavelength and sensing plane) cannot be avoided, error in the AO corrector position of as little as 0.5 mm will exacerbate their effects in the rat eye, as shown in Fig. 7. This necessitates precise alignment of the optical system. However, positioning the animal's eye conjugate to the system pupil may not always be optimal, as discussed above. Regardless, it is important to have the ability to translate the animal axially with good precision (in ~0.1 mm steps), as the optimal range of the corrector position may be small, as shown in Figs. 7 and 8. For alignment of the optical system, we recommend the use of a temporary diffraction-limited lens to form a point object that defines the system pupil position. A flat mirror can be used as a proxy for pupil-conjugate components, their relatively low cost allowing a physical knife-edge test to provide precise axial positioning [35].

#165728 - $15.00 USD Received 3 Apr 2012; revised 8 Jun 2012; accepted 14 Jun 2012; published 3 Jul 2012

A final option is to forego wavefront sensing information altogether, or to use it only to obtain a 'ballpark' correction. The remainder of the correction could then be achieved using image-based, or sensor-less, AO [36–39]. This approach involves the addition of random perturbations to the AO corrector and quantification of their effect on image quality, to converge upon the configuration that maximizes image quality. The technique requires far more iterations than conventional AO [36], but this becomes less important in an anaesthetized animal. The technique theoretically circumvents the sources of error described here.

5. Conclusion

Small animal eyes with high numerical aperture promise far greater maximum resolution than human eyes and so offer unprecedented capability for the study of cellular processes *in vivo* with AO. However their high power causes them to suffer from far greater residual aberration in the presence of errors in sensing plane, sensing wavelength, and corrector position. In the combined presence of each of these sources of error, it is possible to offset them against one another to improve image quality, even to the diffraction limit under certain conditions. Other recommended solutions to improve image quality include neutralization of corneal power, the use of scanning systems, correspondence between the plane and wavelength of imaging/sensing, tight control over delivery of sensing light, precise axial alignment of the optical system, and possibly the use of sensorless AO control.

#165728 - $15.00 USD Received 3 Apr 2012; revised 8 Jun 2012; accepted 14 Jun 2012; published 3 Jul 2012